Computationally Efficient MR-FDPF Method for Multifrequency Simulations

Dmitry Umansky, Jean-Marie Gorce, Meiling Luo, Guillaume de la Roche,
Guillaume Villemaud

HAL Id: inria-00621315

https://hal.inria.fr/inria-00621315

Submitted on 10 Sep 2011

R INRIA

Computationally Efficient MR-FDPF Method for Multifrequency Simulations

Dmitry Umansky — Jean-Marie Gorce — Meiling Luo — Guillaume de la Roche —

Guillaume Villemaud

N° 7726

August 2011

*R apport
de recherche*

Computationally Efficient MR-FDPF Method for Multifrequency Simulations

Dmitry Umansky*, Jean-Marie Gorce†, Meiling Luo‡, Guillaume de la Roche§, Guillaume Villemaud¶

Abstract: In this report, we propose a modification of the multi-resolution frequency domain ParFlow (MR-FDPF) method that allows simulating radio propagation channels in a frequency range. The performance of the proposed MR-FDPF implementation has been analyzed based on different realistic propagation scenarios.

Key-words: ParFlow, TLM, wave propagation, indoor radio propagation, channel simulation, multi-resolution, frequency domain, OFDM.

E-mail: (see http://www.citi.insa-lyon.fr/teams/swing/#people).

* CITI, INSA-LYON, F-69621, Villeurbanne, France, and INRIA, Université de Lyon, F-69621, Villeurbanne, France.
† CITI, INSA-LYON, F-69621, Villeurbanne, France, and INRIA, Université de Lyon, F-69621, Villeurbanne, France.
‡ Ranplan Wireless Network Design Ltd, Suite 25, The Business Competitiveness Centre, Kimpton Road, LU2 0SX, Luton, UK.
§ CWiND, University of Bedfordshire, Park Square Campus, Luton LU1 3JU, UK.
¶ CITI, INSA-LYON, F-69621, Villeurbanne, France, and INRIA, Université de Lyon, F-69621, Villeurbanne, France.

Optimisation de la méthode MR-FDPF pour simulation à multiple fréquences

Résumé : Dans ce rapport nous proposons une nouvelle implémentation de la méthode ParFlow multi-résolution (MR-FDPF) permettant de simuler le canal de propagation radio dans une large bande de fréquences. Les performances de la méthode ParFlow implémentée ont été validées dans différents scenarios.

Mots-clés : ParFlow, TLM, propagation des ondes, propagation indoor, simulation de canal, multi-résolution, domaine fréquentiel, OFDM.

1 Introduction

The new generation of wireless communication systems, such as the IEEE 802.16 WiMAX and the 3GPP Long Term Evolution (LTE), has recently come to the stage of actual deployment. Broadband wireless access (BWA) technologies constitute indispensable part of these systems. The orthogonal frequency division multiplexing (OFDM) [1] is one of the key BWA techniques implemented in modern high data rate wireless communication systems.

In order to evaluate and optimize the performance of OFDM systems, reliable models that adequately describe radio propagation channels over the whole system frequency bandwidth are required. The deterministic channel models based on the numerical simulation of the Maxwell equations [2], as well as the models based on the ray-optical methods [3], are known for their relatively high accuracy [4]. One of the main drawbacks of these modeling approaches is the large computational load.

During the last decade, a great deal of research has been focused on finding an optimal trade-off between the computational cost and the achievable accuracy of the deterministic channel modeling approaches. In [5], the multi-resolution frequency domain ParFlow (MR-FDPF) method has been proposed. The method has proved to be efficient for modeling indoor and indoor-like environments. However, similar to the majority of the frequency domain methods [6–8], the MR-FDPF algorithm has to be repeated for every frequency in the range of interest. Consequently, the computational cost associated with applying the method quickly becomes excessively large as the number of frequencies increases. This is particularly the case for OFDM wireless communication systems, where data is transmitted in parallel over several sub-carriers.

further development of the MR-FDPF method. The proposed modification of the MR-FDPF method allows computationally efficient radio coverage prediction at multiple frequencies. In the traditional implementation of the MR-FDPF method (see, e.g., [5]), simulations of the electromagnetic wave propagation at every single frequency consists of three steps: the *preprocessing step*, the *upward step*, and the *downward step*. The *preprocessing step* is by far the most demanding step of the MR-FDPF method in terms of the computational resources. The computational efficiency of the modified MR-FDPF method is achieved by conducting the *preprocessing step* only once during simulations of the wave propagation in a range of frequencies.

The rest of the report is organized as follows. Section 2, gives a general overview of the MR-FDPF method. In Section 3, we describe the proposed modification of the MR-FDPF method for channel modeling in OFDM systems. The results of the performance analysis for the proposed implementation of the MR-FDPF method are presented in Section 4. The concluding remarks are given in Section **??**.

Figure 1: Incident and reflected flows.

2 MR-FDPF Method

In this section, a general overview of the MR-FDPF method is provided in order to facilitate the presentation of the material in Section 3. For additional details, an interested reader is addressed to [5, 9, 10].

2.1 ParFlow Formulation

The ParFlow (or, more exactly, the time domain ParFlow) method is based on the cellular automata formalism [11–14]. In this method, the scalar electrical field strength is obtained by summing the fictitious flows traveling along a regular grid of connection lines and experiencing scattering at the nodes of the grid (see Fig. 1).

At every node r of the grid, the discrete time evolution of the flows is described by the equation

$$\overrightarrow{\mathbf{F}}(r,t) = \mathbf{W}(r)\overleftarrow{\mathbf{F}}(r, t - \triangle t) + \overrightarrow{\mathbf{S}}(r,t) \tag{1}$$

where the incident (inward) flows vector $\overleftarrow{\mathbf{F}}(r,t)$, the reflected (outward) flows vector $\overrightarrow{\mathbf{F}}(r,t)$, and the source flows vector $\overrightarrow{\mathbf{S}}(r,t)$ are defined, respectively, as follows

$$
\begin{aligned}
\overleftarrow{\mathbf{F}}(r,t) &= \left[\overleftarrow{f}_E(r,t)\,\overleftarrow{f}_W(r,t)\,\overleftarrow{f}_S(r,t)\,\overleftarrow{f}_N(r,t)\,\breve{f}_0(r,t)\right]^T \\
\overrightarrow{\mathbf{F}}(r,t) &= \left[\overrightarrow{f}_E(r,t)\,\overrightarrow{f}_W(r,t)\,\overrightarrow{f}_S(r,t)\,\overrightarrow{f}_N(r,t)\,\breve{f}_0(r,t)\right]^T \\
\overrightarrow{\mathbf{S}}(r,t) &= \left[\overrightarrow{s}_E(r,t)\,\overrightarrow{s}_W(r,t)\,\overrightarrow{s}_S(r,t)\,\overrightarrow{s}_N(r,t)\,0\right]^T.
\end{aligned} \tag{2}
$$

The operator $\{\cdot\}^T$ signifies matrix transposition. The inner flow $\breve{f}_0(r,t)$ in (2) models dielectric media with the relative permittivities $\varepsilon_r \neq 1$. Note that the reflected flows at the grid node r correspond to the incident flows at its immediate neighbor nodes, that is

$$\overleftarrow{f}_d(r + \triangle r, t) = \overrightarrow{f}_d(r, t - \triangle t), \quad d \in E, W, S, N \tag{3}$$

where $\triangle r$ is the spatial grid step, which is assumed to be the same along all the coordinate axes. The step $\triangle r$ satisfies the following conditions

$$\triangle r = c_0\sqrt{2}\triangle t, \quad \triangle r \ll \lambda \tag{4}$$

where c_0 denotes the speed of an electromagnetic wave in a propagation medium and λ is the smallest wavelength in the spectrum of the source signal.

The scattering matrix $\mathbf{W}(r)$ in (1) reads as follows

$$
\mathbf{W}(r) = \begin{bmatrix}
1 & \alpha_r & 1 & 1 & Y_r \\
\alpha_r & 1 & 1 & 1 & Y_r \\
1 & 1 & 1 & \alpha_r & Y_r \\
1 & 1 & \alpha_r & 1 & Y_r \\
1 & 1 & 1 & 1 & \beta_r
\end{bmatrix} \tag{5}
$$

where $\alpha_r = 1 - 2n_r^2$; $\beta_r = 2n_r^2 - 4$. The parameters n_r and $Y_r = 4n_r^2 - 4$ denote the refraction index and the local admittance, respectively. In order to satisfy the boundary conditions, the scattering matrix $\mathbf{W}(r)$ must be modified as described, e.g., in [11].

The complex scalar electrical field strength $\Psi(r, t)$ is given by

$$\Psi(r, t) = \frac{1}{n_r^2} \left(Y_r \breve{f}_0 + \sum_{d=E,W,S,N} \overrightarrow{f}_d(r, t) \right). \tag{6}$$

2.2 Multi-Resolution Frequency Domain (MR-FD) Approach

Taking the Fourier transform of both sides of the local scattering equation (1) leads to

$$\overrightarrow{\mathbf{F}}(r, \nu) = \mathbf{W}(r) e^{-j2\pi\nu\triangle t} \overleftarrow{\mathbf{F}}(r, \nu) + \overrightarrow{\mathbf{S}}(r, \nu) \tag{7}$$

where ν denotes the frequency.

By aggregating the incident flow vectors $\overleftarrow{\mathbf{F}}(r, \nu)$ for all nodes into a single incident flow vector $\overleftarrow{\underline{\mathbf{F}}}(\nu)$ and similarly gathering the reflected flow vectors $\overrightarrow{\mathbf{F}}(r, \nu)$ and the source flow vectors $\overrightarrow{\mathbf{S}}(r, \nu)$ into the global flow vectors $\overrightarrow{\underline{\mathbf{F}}}(\nu)$ and $\overrightarrow{\underline{\mathbf{S}}}(\nu)$, respectively, we come to the global scattering equation

$$\overrightarrow{\underline{\mathbf{F}}}(\nu) = \underline{\mathbf{W}} e^{-j2\pi\nu\triangle t} \overleftarrow{\underline{\mathbf{F}}}(\nu) + \overrightarrow{\underline{\mathbf{S}}}(\nu) \tag{8}$$

where $\underline{\mathbf{W}}$ is the global scattering matrix obtained by properly combining the local scattering matrices $\mathbf{W}(r)$ defined in (5).

Taking into account the relationship between the incident and the reflected flows of the adjacent nodes expressed by (3), equation (8) can be rewritten in terms of the reflected flow vector[1] $\overrightarrow{\underline{\mathbf{F}}}(\nu)$ as

$$\overrightarrow{\underline{\mathbf{F}}}(\nu) = \widetilde{\underline{\mathbf{W}}} e^{-j2\pi\nu\triangle t} \overrightarrow{\underline{\mathbf{F}}}(\nu) + \overrightarrow{\underline{\mathbf{S}}}(\nu) \tag{9}$$

where the matrix $\widetilde{\underline{\mathbf{W}}}$ signifies a permutated global scattering matrix $\underline{\mathbf{W}}$.

The solution to equation (9) can now be found as

$$\overrightarrow{\underline{\mathbf{F}}}(\nu) = \left(\mathbf{I} - \widetilde{\underline{\mathbf{W}}} e^{-j2\pi\nu\triangle t} \right)^{-1} \overrightarrow{\underline{\mathbf{S}}}(\nu) \tag{10}$$

where $\mathbf{I}$ denotes the identity matrix.

The multi-resolution approach [5] provides a computationally efficient way of solving the equation (9). The approach is based on combining all the grid nodes into a single large head node that encompasses the considered propagation environment. After imposing prespecified boundary conditions, the head node is decomposed back into the original grid nodes. The process of applying the multi-resolution approach is divided into three steps: *preprocessing step*, *upward step*, and *downward step*. Further details related to the implementation of the MF-FD approach can be found in [5, 9]. Here, it is sufficient to mention that the highest computational load is associated with the *preprocessing step*. For a propagation environment of dimensions $M \times M$ nodes the computational loads for the *preprocessing step*, the *upward step*, and the *downward step* are estimated as [9]:

---

[1] Similarly, equation (8) can be reformulated in terms of the incident flow vector $\overleftarrow{\underline{\mathbf{F}}}(\nu)$.

- *preprocessing step*: $O\{52 \cdot M^3\}$;

- *upward step*[2]: $O\{3 \cdot M^2\}$;

- *downward step*: $O\{10 \cdot \log_2(M) \cdot M^2\}$.

---

[2]The computational cost is given per signal source.

3 Optimization of MR-FDPF method for multifrequency simulations

A major limitation of the MR-FD approach is that it provides a solution $\overrightarrow{\underline{\mathbf{F}}}(\nu)$(or, equivalently, $\overleftarrow{\underline{\mathbf{F}}}(\nu)$) of the global scattering equation (9) only at one frequency ν. That means that the MR-FDPF method has to be applied repeatedly at every frequency point in the range of interest B, e.g., for every sub-channel carrier frequency in OFDM communication systems.

In this section, a computationally efficient implementation of the MR-FDPF method is presented. The proposed implementation allows for a significant reduction in the computational load as compared to a straightforward repetition of the MR-FDPF method at multiple frequencies at the cost of acceptable degradation of the accuracy in predicting the electromagnetic wave propagation.

Without any loss of generality, we consider that only one signal source is present. Thus, we can also assume $\overrightarrow{\underline{\mathbf{S}}}(\nu) = \overrightarrow{\underline{\mathbf{S}}} \neq 0$), for all $\nu \in B$. If it is not the case, both sides of equation (10) can always be multiplied by a correction scalar factor.

A solution (10) of equation (9) at the frequency $\nu_0 \in B$ is given by

$$\overrightarrow{\underline{\mathbf{F}}}(\nu_0) = \left(\mathbf{I} - \widetilde{\underline{\mathbf{W}}}(\nu_0)\right)^{-1} \overrightarrow{\underline{\mathbf{S}}} \tag{11}$$

where $\widetilde{\underline{\mathbf{W}}}(\nu_0) = \widetilde{\underline{\mathbf{W}}} e^{-j2\pi\nu_0\triangle t}$. Similar expression for the frequency $\nu_0 + \triangle\nu$ reads as

$$\overrightarrow{\underline{\mathbf{F}}}(\nu_0 + \triangle\nu) = \left(\mathbf{I} - \widetilde{\underline{\mathbf{W}}}(\nu_0 + \triangle\nu)\right)^{-1} \overrightarrow{\underline{\mathbf{S}}}. \tag{12}$$

Note that $\widetilde{\underline{\mathbf{W}}}(\nu_0 + \triangle\nu) = e^{-j2\pi\triangle\nu\triangle t}\widetilde{\underline{\mathbf{W}}}(\nu_0)$. Equation (12) can be rewritten as

$$\overrightarrow{\underline{\mathbf{F}}}(\nu_0 + \triangle\nu) = \left(\mathbf{I} - \widetilde{\underline{\mathbf{W}}}(\nu_0) + \widetilde{\underline{\mathbf{W}}}(\nu_0) - e^{-j2\pi\triangle\nu\triangle t}\widetilde{\underline{\mathbf{W}}}(\nu_0)\right)^{-1} \overrightarrow{\underline{\mathbf{S}}} \tag{13}$$

After inserting (11) into (13) we obtain

$$\overrightarrow{\underline{\mathbf{F}}}(\nu_0 + \triangle\nu) = \left(\mathbf{I} - \left(\mathbf{I} - \widetilde{\underline{\mathbf{W}}}(\nu_0)\right)^{-1} \widetilde{\underline{\mathbf{W}}}_{\triangle\nu}\right)^{-1} \overrightarrow{\underline{\mathbf{F}}}(\nu_0) \tag{14}$$

where the matrix $\widetilde{\underline{\mathbf{W}}}_{\triangle\nu} = (e^{-j2\pi\triangle\nu\triangle t} - 1)\widetilde{\underline{\mathbf{W}}}(\nu_0)$.

Using the Neumann series expansion (see, e.g., [15]) we can write

$$\overrightarrow{\underline{\mathbf{F}}}(\nu_0 + \triangle\nu) = \left(\sum_{n=0}^{\infty} \left[\left(\mathbf{I} - \widetilde{\underline{\mathbf{W}}}(\nu_0)\right)^{-1} \widetilde{\underline{\mathbf{W}}}_{\triangle\nu}\right]^n\right) \overrightarrow{\underline{\mathbf{F}}}(\nu_0) \tag{15}$$

where it is implied that $\mathbf{A}^0 = \mathbf{I}$ for any square matrix $\mathbf{A}$.

According to (15), an N-th order approximation of (12) is given by

$$\overrightarrow{\underline{\mathbf{F}}}(\nu_0 + \triangle\nu) \approx \overrightarrow{\underline{\mathbf{F}}}(\nu_0) + \overrightarrow{\underline{\mathbf{F}}}^{(1)}(\triangle\nu) + \ldots + \overrightarrow{\underline{\mathbf{F}}}^{(N)}(\triangle\nu) \tag{16}$$

where

$$\overrightarrow{\underline{\mathbf{F}}}^{(1)}(\triangle\nu) = \left(\mathbf{I} - \widetilde{\underline{\mathbf{W}}}(\nu_0)\right)^{-1} \widetilde{\underline{\mathbf{W}}}_{\triangle\nu} \overrightarrow{\underline{\mathbf{F}}}(\nu_0) \tag{17}$$

and

$$\overrightarrow{\underline{\mathbf{F}}}^{(n+1)}(\triangle\nu) = \left(\mathbf{I} - \widetilde{\underline{\mathbf{W}}}(\nu_0)\right)^{-1} \widetilde{\underline{\mathbf{W}}}_{\triangle\nu} \overrightarrow{\underline{\mathbf{F}}}^{(n)}(\triangle\nu) \tag{18}$$

It is worth noticing that (18) (as well as (17)) is similar to (11). The only difference is that the source vector $\overrightarrow{\underline{\mathbf{S}}}$ in (11) is substituted by the vector $\widetilde{\underline{\mathbf{W}}}_{\triangle\nu} \overrightarrow{\underline{\mathbf{F}}}^{(n)}(\triangle\nu)$ in (18). Thus, the MR-FDPF method can readily be applied in order to find the vector $\overrightarrow{\underline{\mathbf{F}}}^{(n+1)}(\triangle\nu)$ in (18).

An important question is the convergence speed of the approximation (16). A sufficient condition for the convergence of the Neumann series is that the spectral radius of the matrix $\left(\mathbf{I} - \widetilde{\underline{\mathbf{W}}}(\nu_0)\right)^{-1} (e^{-j2\pi\triangle\nu\triangle t} - 1)\underline{\mathbf{W}}(\nu_0)$ is less than 1 [15]. Based on the fact that in practice, the eigenvalues of the scattering matrix $\widetilde{\underline{\mathbf{W}}}(\nu)$ must be real and smaller than 1, it can be induced that the smaller the spectral radius of the matrix $\widetilde{\underline{\mathbf{W}}}(\nu)$ (or, in different words, the larger the attenuation due to the propagation environment), the faster is the convergence of the approximation (16).

The advantage of using the approximation (16) lies in the fact that the scattering matrix $\widetilde{\underline{\mathbf{W}}}(\nu)$ is calculated only for the frequency ν_0. That means that the *preprocessing step* (see [5,9]), which is the most computationally expensive one, is conducted only once. On the downside, however, equation (18) implies that while calculating the terms $\overrightarrow{\underline{\mathbf{F}}}^{(n)}(\triangle\nu)$, $n = 1, 2, \ldots$, each node is a signal source. Thus, the computational cost of the *upward step* for each additional term $\overrightarrow{\underline{\mathbf{F}}}^{(n)}(\triangle\nu)$ becomes $O\{\log_2(M)M^2\}$ (up to a constant scaling factor). Of course, the additional computational loads associated with the *upward step* and the *downward step* are linearly proportional to the number of terms N in the approximation (16). Nevertheless, for large propagation environments (large M), the computational cost of the *preprocessing step* is dominating, hence the approximate solution (16) promises significant computational savings.

In Section 4, we assess the performance of the proposed MR-FDPF method implementation based on the simulation results obtained for two propagation scenarios.
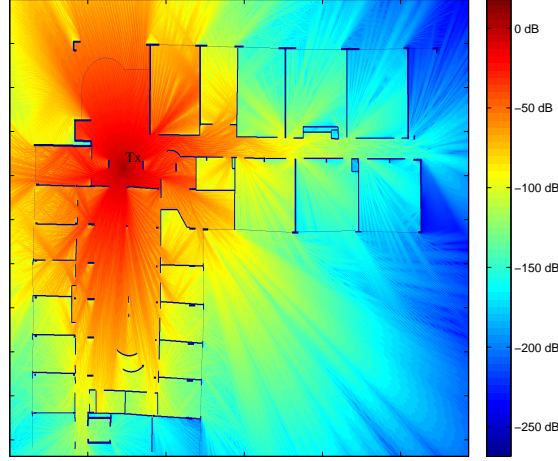
Figure 2: Radio coverage prediction inside the CITI building at $\nu = 2.345$ GHz.

4   Experimental Results

In this section, we present the results of applying the proposed implementation of the MR-FDPF approach to predicting radio coverage in two realistic propagation scenarios. Unfortunately, we are not able to provide any experimental results for the MR-FDTLM method described in Section **??** as, presently, no TLM based prediction tool is at our disposal.

The first propagation scenario is inside the CITI building, INSA university campus in Lyon. The building dimensions are approximately 40×60 m. The electrical field strength $\Psi(r, \nu)$ inside the CITI building and its immediate surroundings has been computed with a spatial resolution of 2 cm. In Fig. 2, the power $P(r, \nu)$ of the electrical field predicted by the MR-FDPF method at the frequency $\nu = 2.345$ GHz is depicted. The position of the omnidirectional transmitting antenna is indicated in Fig. 2.

We are to compare the electric field power $\hat{P}(r, \nu)$ predicted with the MR-FDPF method optimized for multifrequency simulations as described in Section 3 to the electric field power $P(r, \nu)$ predicted with the traditional implementation of the MR-FDPF method, i.e., the implementation where the *preprocessing step* takes place at every frequency ν.

In the following, the elapsed time it takes to complete the *preprocessing step* is referred to as the preprocessing time. In a similar manner, the time period spent on the radio coverage prediction, i.e., the *upward step* together with the *downward step*, is called the prediction time. For the traditional MR-FDPF implementation, the total preprocessing time T_{prepr} and the total prediction time T_{pred} are $K \cdot 620$ s and $K \cdot 40$ s, respectively, where K is the number of frequencies. For the proposed implementation of the MR-FDPF method optimized for multifrequency simulations, the total preprocessing time is $T_{\text{prepr}} = 620$ s, while the total prediction time is given by $T_{\text{pred}} = K \cdot 40 \cdot k$. The factor k depends on the chosen number of terms N in the approximation (16). For example, $k = 5.7, 10.2$, and 15.66 for $N = 1, 2$, and 3, respectively.
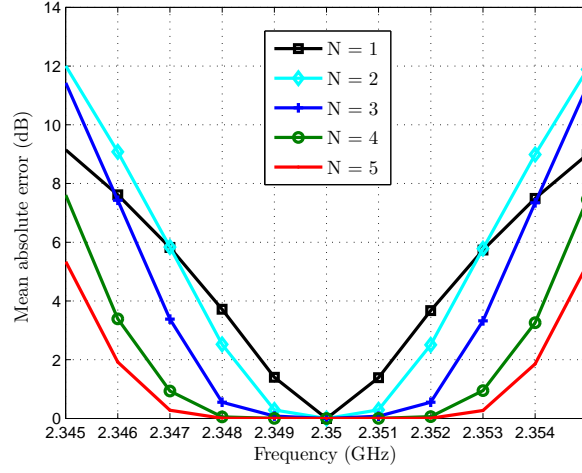
Figure 3: CITI. Average approximation error ($\nu_0 = 2.35$ GHz).
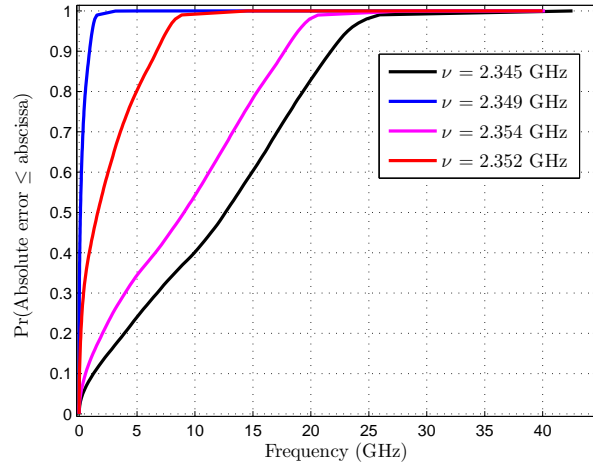
Figure 4: CITI. CDF of the absolute approximation error $N = 2$ ($\nu_0 = 2.35$ GHz).

The mean absolute approximation error $|\hat{P}(r,\nu)[dBm] - P(r,\nu)[dBm]|$ for several numbers of terms N in (16) is shown in Fig. 3. In Figs. 4 and 5, examples of the cumulative distributions functions (CDFs) of the absolute approximation error are shown for several frequencies ν and several numbers of terms N, respectively. As expected, a larger deviation $\triangle\nu$ from the central frequency ν_0 causes the approximation error to expand. Also, as the number of terms N in (16) increases, the approximation error decreases, or, alternatively, we observe expansion of the frequency band, in which the error is bounded by a certain level. For example, the mean approximation error is bounded by 3 dB in the frequency range of 3 MHz, 4 MHz for $N = 1$, $N = 2$ terms, respectively.
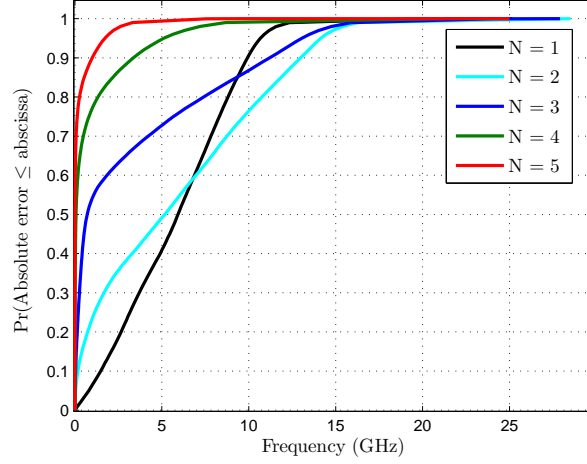
Figure 5: CITI. CDF of the absolute approximation error $\nu = 2.347$ GHz ($\nu_0 = 2.35$ GHz).

Based on the electrical field strength $\Psi(r, \nu)$ predicted with the MR-FDPF implementations at the frequencies $\nu = 2.345, 2.346 \ldots, 2.355$ GHz, the delay spread has been estimated at 100 randomly selected positions. The chosen positions satisfy the condition that the approximation error is lower than 3 dB at the frequency $\nu = 2.345$ GHz. In order to improve the estimate of the delay spread, the assessed power delay profiles (PDPs) have been averaged over 7×7 - point regions centered at the selected positions. The estimated delay spreads for the considered realizations of the MR-FDPF method are demonstrated in Fig. 6. In the figure, the red dashed line corresponds to the perfect match between the estimated delay spreads. Note that for larger delay spreads, the values obtained with the MR-FDPF method optimized for multifrequency simulations are slightly overestimated as compared to the delay spreads determined with the traditional implementation of the MR-FDPF method. The average relative absolute error is equal to 0.048.

Figure 7 demonstrates the spatial distribution of the approximation error at the frequency $\nu = 2.347$ GHz provided by the $N = 2$ term approximation. Note that the extreme values of the approximation error appear only at a limited number of points at the border of the propagation environment. It can also be seen from Fig. 7 that there exists a correlation between the predicted power $P(r, \nu)$ and the approximation error. Indeed, the smaller the power $P(r, \nu)$, the larger is the approximation error $|\hat{P}(r, \nu)[dBm] - P(r, \nu)[dBm]|$. This observation is supported by the plot in Fig. 8, which illustrates the distribution of the observation points with respect to (w.r.t.) the predicted power $P(r, \nu)$ and the absolute approximation error.

The second propagation scenario is an indoor office environment in Stanford University. The dimensions of the environment are approximately 16×34 m. The positions of 8 transmitters equipped with omnidirectional antennas are depicted in Fig. 9. The electrical field strength $\Psi(r, \nu)$ has been calculated with the 2 cm spatial resolution.

The power $P(r, \nu)$ of the electrical field predicted by the MR-FDPF method at the frequency $\nu = 2.345$ GHz is shown in Fig. 10.
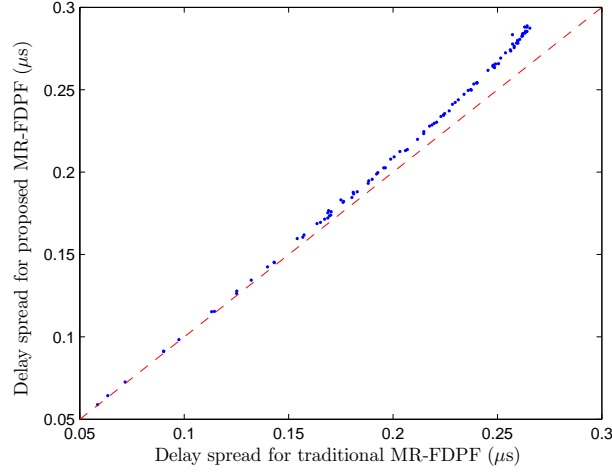
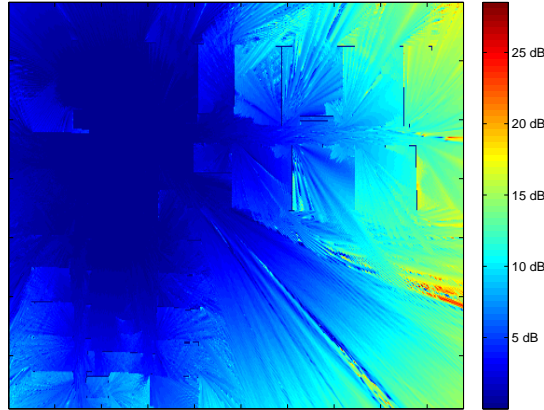Figure 6: CITI. Estimated delay spread $N = 2$ ($\nu_0 = 2.35$ GHz).

Figure 7: CITI. Spatial distribution of the approximation error at $\nu = 2.347$ GHz and $N = 2$ ($\nu_0 = 2.35$ GHz).

The total preprocessing time for the MR-FDPF method optimized for multifrequency simulations is approximately $T_{\text{prepr}} = 96$ s. The total prediction time equals $T_{\text{pred}} = K \cdot 11 \cdot k$ s, where $k = 4.24$, 7.32, and 10.10 for $N = 1$, 2, and 3, respectively.

In Fig. 11, the mean approximation errors $|\hat{P}(r, \nu)[dBm] - P(r, \nu)[dBm]|$ for all the transmitters are presented, respectively. Here, the number of terms N in (16) equals 2. Depending on the transmitter location, the frequency bandwidth corresponding to the 3 dB mean approximation error varies in the range 3 to 5 MHz. The examples of the CDFs of the absolute approximation error are shown in Fig. 12.

The delay spreads estimated with the MR-FDPF realizations for the considered propagation environment are depicted in Fig. 13. Again, the delay spreads have been
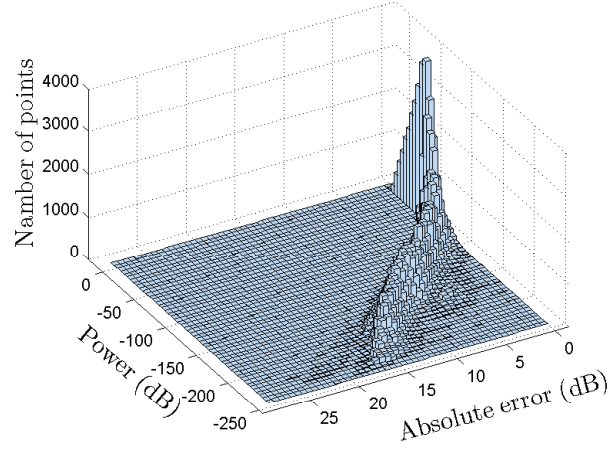
Figure 8: CITI. Distribution of the observation points w.r.t. the predicted power and the absolute approximation error ($\nu = 2.347$ GHz, $N = 2$, $\nu_0 = 2.35$ GHz).
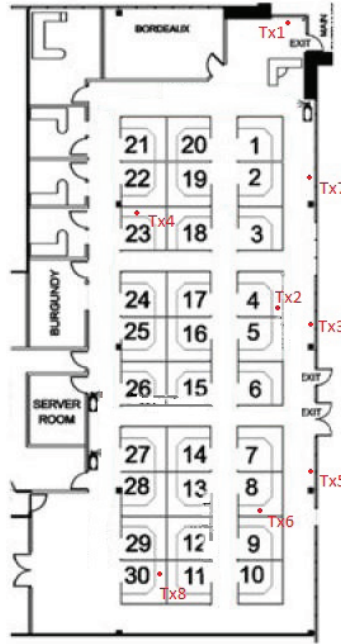

Figure 9: Stanford. Propagation environment.

estimated at 100 randomly selected positions satisfying the condition that the approximation error is lower than 3 dB at the frequency $\nu = 2.345$ GHz. The average relative absolute error between the estimated delay spreads in Fig. 13 is 0.082.

A spatial distribution of the approximation error for the transmitter Tx 6 at the frequency $\nu = 2.347$ GHz provided by the $N = 2$ term approximation is shown in
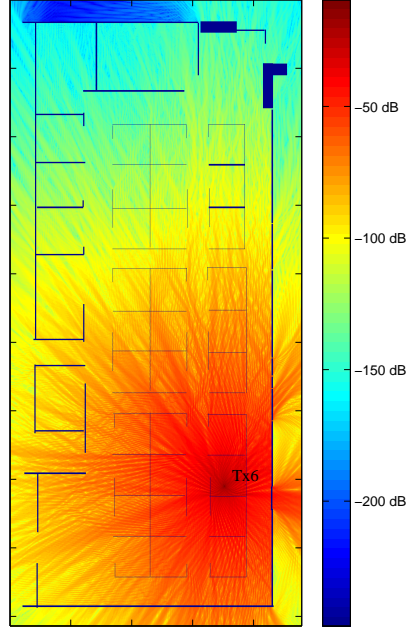
Figure 10: Stanford. Radio coverage prediction for Tx 6 at $\nu = 2.345$ GHz.
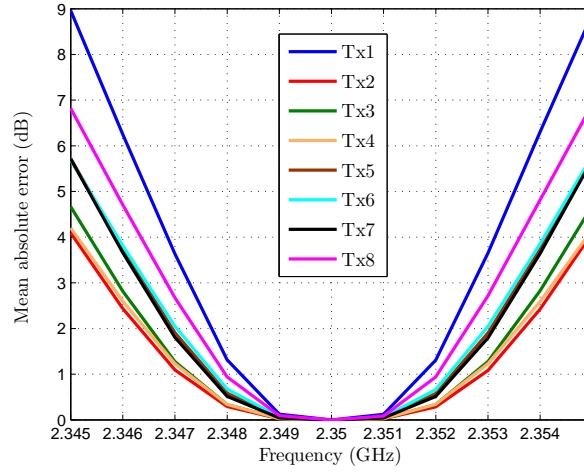
Figure 11: Stanford. Average approximation error ($N = 2$, $\nu_0 = 2.35$ GHz).

Fig. 14. Similar to the CITI propagation scenario considered above (although, less evident), the approximation error is lower at the points where the predicted power $P(r, \nu)$ is relatively larger (*cf.* the results presented in Fig. 7). The relationship between the
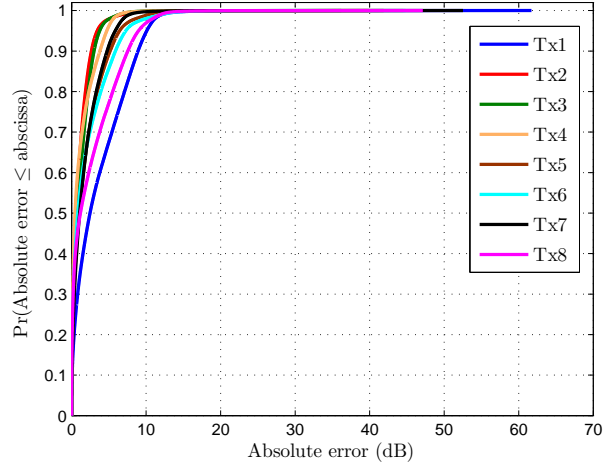
Figure 12: Stanford. CDF of the absolute approximation error ($N = 2$, $\nu = 2.345$ GHz, $\nu_0 = 2.35$ GHz).
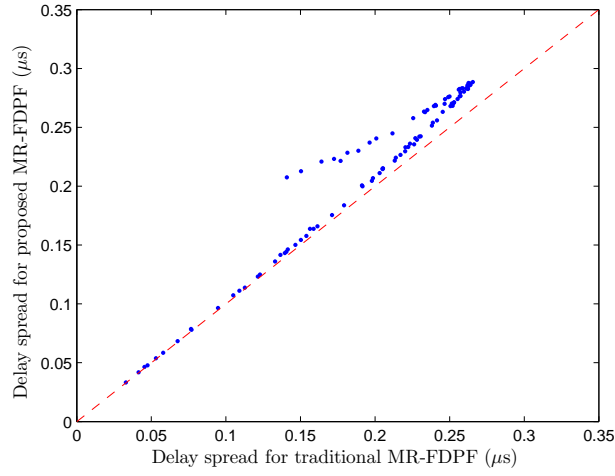
Figure 13: Stanford. Estimated delay spread $N = 2$, ($\nu_0 = 2.35$ GHz).

absolute approximation error and the predicted power for the considered propagation environment is illustrated by the bivariate histogram in Fig. 15.
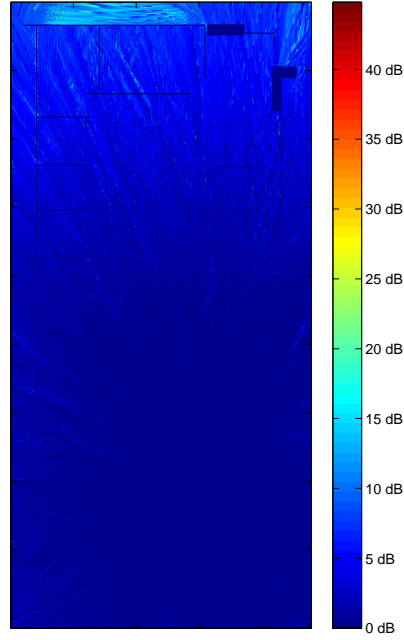
Figure 14: Stanford. Spatial distribution of the approximation error for TX 6 at $\nu = 2.347$ GHz and $N = 2$ ($\nu_0 = 2.35$ GHz).
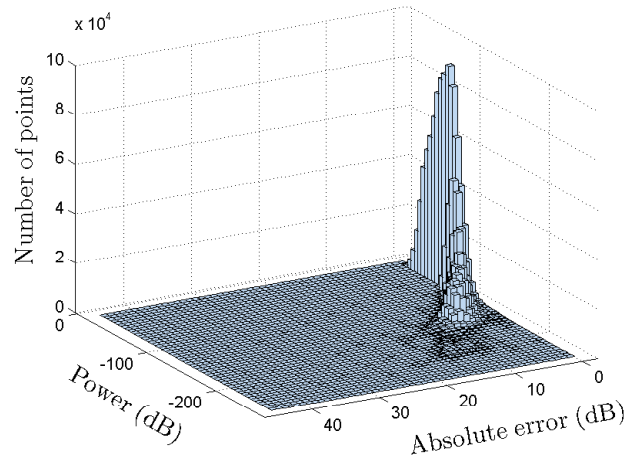
Figure 15: Stanford. Distribution of the observation points w.r.t. the predicted power and the absolute approximation error ($\nu = 2.347$ GHz, $N = 2$, $\nu_0 = 2.35$ GHz).

5   Conclusion

In this report, a new implementation of the MR-FDPF method optimized for multifrequency simulations has been presented. The described implementation can reduce the computational cost of the radio coverage prediction at multiple frequencies as compared to the traditional MR-FDPF method.

Experimental results provided in this paper demonstrate that the proposed implementation of the MR-FDPF method predicts the radio coverage in a range of frequencies with acceptable accuracy and without excessive computational overload. In general, the accuracy of the prediction or, alternatively, the frequency bandwidth, in which a specified accuracy is sustained, is dependent on the modeled propagation environment. It has been noticed that the prediction accuracy degrades as the distance from the transmitter increases.

References

[1] U. S. Jha and R. Prasad, *OFDM. Towards Fixed and Mobile Broadband Wireless Access*. Artech House, 2007.

[2] J. Daniel G. Swanson and W. J. R. Hoefer, *Microwave Circuit Modeling Using Electromagnetic Field Simulation*. Artech House, 2003.

[3] R. Hoppe, P. Wertz, F. M. Landstorfer, and G. Wölfle, "Advanced ray-optical wave propagation modelling for urban and indoor scenarious including wideband properties," *Europian Transactions on Telecommunications*, vol. 14, pp. 61–69, 2003.

[4] A. F. Molisch, *Wireless Communications*. Chichester: Wiley-IEEE Press, 2005.

[5] J.-M. Gorce, K. Jaffrès Runser, and G. De La Roche, "The Adaptive Multi-Resolution Frequency-Domain ParFlow (MR-FDPF) Method for Indoor Radio Wave Propagation Simulation. Part I : Theory and Algorithms," INRIA, Tech. Rep. RR-5740, 11 2005. [Online]. Available: http://hal.inria.fr/inria-00070278/PDF/RR-5740.pdf

[6] P. Berini and K. Wu, "A new frequency domain symmetrical condensed tlm node," *IEEE Microw. Guided Wave Lett.*, vol. 4, no. 6, pp. 180–182, 1994.

[7] D. Johns and C. Christopouros, "New frequency-domain tlm method for the numerical solution of steady-state electromagnetic problems," *IEE Proceedings - Science, Measurement and Technology*, vol. 141, no. 4, pp. 310–316, 1994.

[8] H. Jin and R. Vahldieck, "A new Frequency-Domain TLM symmetrical condensed node derived directly from Maxwell's equations," in *Proc. IEEE MTT-S Int. Microwave Symp. Digest*, 1995, pp. 487–490.

[9] J.-M. Gorce, K. Jaffres-Runser, and G. de la Roche, "Deterministic approach for fast simulations of indoor radio wave propagation," *IEEE Trans. Antennas Propag.*, vol. 55, no. 3, pp. 938–948, 2007.

[10] G. de la Roche, K. Jaffres-Runser, and J.-M. Gorce, "On predicting in-building WiFi coverage with a fast discrete approach," *International Journal of Mobile Network Design and Innovation*, vol. 2, pp. 3–12, 2007.

[11] B. Chopard, P. Luthi, and J.-F. Wagen, "Lattice-Boltzmann method for wave propagation in urban microcells," *Microwaves, Antennas and Propagation, IEE Proceedings*, vol. 144, no. 4, pp. 251 –255, aug 1997.

[12] B. Chopard and M. Droz, *Cellular Automata Modeling of Physical Systems*. Canbridge University Press, 1998.

[13] P. O. Luthi, "Lattice wave automata: From radio waves to fractures propagation," Ph.D. dissertation, University of Geneva, 1998.

[14] B. Chopard and P. O. Luthi, "Lattice-Boltzmann computations and applications to physics," *Theor. Comput. Sci.*, vol. 217, no. 1, pp. 115–130, 1999.

[15] C. D. Meyer, *Matrix Analysis and Applied Linear Algebra*. SIAM, 2001.

Contents